Mechanism Optimization of A New Integrated Leg for Legged Robots

Yansong Song, Xinyu Zhao, Xianyue Gang, Hui Chai, Peng Fu

***Abstract*—The leg mechanism holds considerable significance for the load-bearing and lightweight design of legged robots. Herein, an integrated leg system was constructed to address the instability challenges in extreme operational environments. Utilizing the vector algebra and linear transformation methods, the explicit geometric analysis equations and quasi-static force balance equations for the leg mechanism were established. Subsequently, an optimization model was proposed with the coordinates of joint points as the design variables, leading to an optimized structural layout for the leg mechanism. The results show that the optimized leg mechanism effectively reduces the peak force of the hydraulic cylinder, thereby enhancing its extreme load-bearing capacity.**

***Index Terms*—legged robot, integrated leg, mechanism optimization, minimize maximum**

I. Introduction

FOR dynamic working environments, legged robots demonstrate versatility by traversing diverse terrains with adept detection and obstacle avoidance capabilities [1]. Hydraulically driven legged robots, as an important robot type, boost advantages of high power density and strong adaptability compared to other drive methods [2]. In this case, legged robots have attracted considerable academic attention worldwide. Specifically, Mosher [3] introduced the world's first hydraulic-driven quadruped robot known as "Walking Truck", opening up a new path for the development of hydraulic-driven robots. Representatives such as robots including BigDog and Atlas developed by Boston Dynamic, and HyQ developed by the Italian Institute of Technology were introduced in [4]-[7].

In recent years, numerous universities and research institutes have conducted extensive research on hydraulic-driven legged robots. For instance, hydraulic-driven legged robotic platforms equipped with mobile power sources have been developed by Harbin Institute of Technology [8]-[9], National University of Defense Technology [10], and Beijing University of Technology [11].

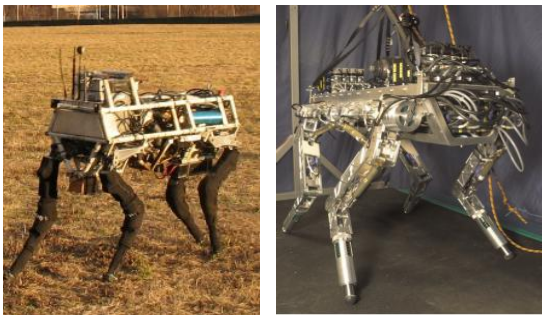

Fig. 1 BigDog and HyQ robots

These platforms are highlighted for their excellent adaptability to non-standard road conditions. Grounded in existing research regarding quadruped robots and biomimetic motion, various hydraulic-driven quadruped robots with certain field operation capability, such as SCalf and SCalf-II, have been developed by the Robotics Research Center of Shandong University [12].

The leg mechanism serves as the cornerstone for controlling both the gait and stability of the entire legged robot system [13]-[14]. The Robotics Research Center of Shandong University has recently proposed an innovative approach to cylinder-leg integration (Fig. 2). This solution streamlines the hydraulic circuitry of the robot and achieves a reduction in mass by incorporating the hydraulic cylinders directly within the framework. Zong [15] has found that single-leg weight reduction can be as significant as 10%. However, the compact design of the leg mechanism can result in suboptimal performance, particularly under extreme working conditions such as navigating steep slopes or initiating movement from a prone position.

Herein, the kinematic and quasi-static dynamics analyses of the new integrated leg mechanism were initially carried out. Then, the objective function, optimization variables, and design constraints, such as spatial dimensions and motion interference, were determined [16]. Ultimately, the kinematic and quasi-static dynamic analyses were integrated into an optimization algorithm to reduce the peak force of the hydraulic cylinders [17].

The remaining part of the paper is organized as follows. Section II presents the integrated leg mechanism and its connection. Section III summarizes the integrated leg linkage configuration and conducts a corresponding geometric analysis. Section IV introduces the quasi-static dynamic

Manuscript received December 27, 2023; revised April 27, 2024. This work was supported in part by the Major Science and Technology Innovation Projects in Shandong under Grant 2019JZZY020317, the National Natural Science Foundation Project of China under Grant 62073191, the Natural Science Foundation of Shandong under Grant ZR2020ME140.

Yansong Song is a graduate of School of Transportation and Vehicle Engineering, Shandong University of Technology, Zibo, 255000 PR China. (e-mail: songys199891@163.com).

Xinyu Zhao is a graduate of School of Transportation and Vehicle Engineering, Shandong University of Technology, Zibo, 255000 PR China. (e-mail: zhaoxinyu7419@163.com).

Xianyue Gang is a Professor of School of Transportation and Vehicle Engineering, Shandong University of Technology, Zibo, 255000 PR China. (corresponding author to provide phone: 86-15092331350; e-mail: gangxianyue@sdut.edu.cn).

Hui Chai is a Professor of School of Robot Research Center, Shandong University, JiNan, 250000 PR China. e-mail: chaimax@sdu.edu.cn).

Peng Fu is a Professor of School of Robot Research Center, Shandong University, JiNan, 250000 PR China. e-mail: fupeng0038@gmail.com).

analysis of the integrated leg linkage configuration. Section V establishes the optimization model for the integrated leg mechanism. Section VI illustrates the effectiveness of the mechanism optimization by presenting a case study. Section VII introduces the suspended swing experiment of the integrated leg, verifying the effectiveness of the mechanism optimization. Section VIII concludes the entire article.

II. INTEGRATED LEG MECHANISM

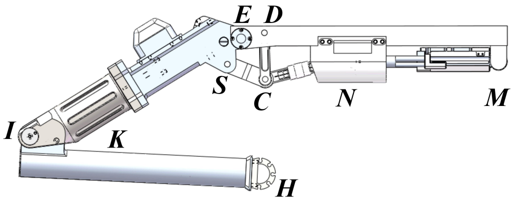

Fig. 2 Integrated single-leg mechanism diagram

The integrated leg mechanism, as depicted in Fig. 2. The hinge points *D*, *C*, *S*, and *E* form the hip joint of the leg mechanism. Among them, hinge points *D* and *E* are hinged to the frame. The end point *M* of the hydraulic cylinder *MN* is hinged on the frame, and the end point *N* is connected to the hip joint. The horizontal movement of the hydraulic cylinder *MN* drove the thigh to achieve oscillation. The hinge points *I*, *J*, and *K* form the knee joint of the leg mechanism, enabling the movement of the shank. This single-leg mechanism boasted two active degrees of freedom (DOFs).

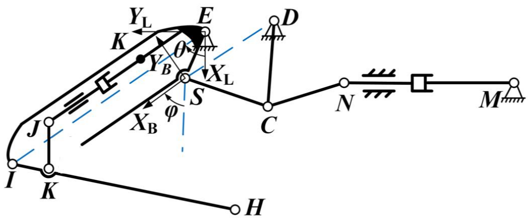

Fig. 3 Integrated leg linkage configuration

III. KINEMATIC GEOMETRY ANALYSIS

The integrated leg linkage configuration is shown in Fig. 3. The global coordinate system xEy took the joint point *E* as the origin, vertically downward as the positive direction of the x-axis, and horizontally to the left as the positive direction of the y-axis. The positive direction of the z-axis was hereby determined by the right-hand rule. To solve the coordinates of each hinge point, the swing angle θ between the positive direction of the x-axis and *EI* was taken as a input parameter to construct the functional relationship between the coordinates of each joint point and the swing angle θ.

The coordinates of joint point *I* were determined form swing angle θ:

$$\begin{Bmatrix} x_I \\ y_I \end{Bmatrix}_G = L_{EI} \begin{Bmatrix} \cos\theta \\ \sin\theta \end{Bmatrix} \tag{1}$$

where the subscript "G" represents the global coordinate system xEy.

The included angle α between *ES* and *EI* is obtained from the distance between *S*, *E* and *I*, and then the coordinates of joint point *S* are:

$$\begin{Bmatrix} x_S \\ y_S \end{Bmatrix}_G = L_{ES} \begin{Bmatrix} \cos(\theta\text{-}\alpha) \\ \sin(\theta\text{-}\alpha) \end{Bmatrix} \tag{2}$$

As shown in Fig. 3, a body coordinate system $x_B F y_B$ was established by taking joint point *S* as the origin, *DS* as the horizontal axis, and the straight line perpendicular to *DS* as the vertical axis. φ denotes the rotation angle from the positive direction of the x-axis of the global coordinate system xEy to *DS*. It could be derived from the coordinates of joint point *S* and joint point *D* as:

$$\cos\varphi = \frac{x_S - x_D}{L_{DS}} \tag{3}$$

$$\sin\varphi = \sqrt{1-\cos^2\varphi} \tag{4}$$

Given the distances between *C*, *D*, and *S* in the retracted state of hydraulic cylinders, the included angle β between *CS* and *DS* can be derived. In the body coordinate system $x_B F y_B$, the coordinates of joint point *C* can be derived by knowing L_{CS}, β:

$$\begin{Bmatrix} x_C \\ y_C \end{Bmatrix}_B = -L_{CS} \begin{Bmatrix} \cos\beta \\ \sin\beta \end{Bmatrix} \tag{5}$$

where the subscript "B" represents the body coordinate system $x_B F y_B$.

Then, the coordinates of joint point *C* in the global coordinate system xEy are derived according to the coordinate transformation equation:

$$\begin{Bmatrix} x_C \\ y_C \end{Bmatrix}_G = \begin{Bmatrix} x_F \\ y_F \end{Bmatrix}_G + \begin{pmatrix} \cos\varphi & -\sin\varphi \\ \sin\varphi & \cos\varphi \end{pmatrix} \begin{Bmatrix} x_C \\ y_C \end{Bmatrix}_B \tag{6}$$

The coordinates of joint point *N* can be obtained according to the Pythagorean Theorem:

$$\begin{Bmatrix} x_N \\ y_N \end{Bmatrix}_G = \begin{Bmatrix} x_N \\ y_C - \sqrt{L_{NC}^2 - (x_C - x_N)^2} \end{Bmatrix} \tag{7}$$

where x_N is a constant, because the hydraulic cylinder *MN* can only move horizontally.

Eqs. (1-7) were explicitly formulated, allowing for the direct determination of the geometric coordinates of the specified points, without solving the equations or calculating their roots.

IV. QUASI-STATIC DYNAMIC ANALYSIS

To establish the quasi-static mechanical equilibrium equations, the moment M_E driving the thigh *ESI* was employed as the input, while the force of the hydraulic cylinder *MN* was adopted as the output for simplicity.

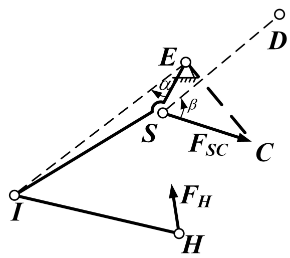

Fig. 4 Thigh force analysis diagram

As shown in Fig. 4, F_H represents the force on the foot in vertical plane. Taking the thigh *ESI* and the connecting rod

CS as a whole, the moment equilibrium equation was established for point *E,* and the force F_{CS} could be obtained as:

$$F_{CS} = -\frac{M_E}{\left\| \boldsymbol{EC} \times \boldsymbol{n_{CS}} \right\|_2} \tag{8}$$

where M_E indicates the magnitude of the driving moment applied to the joint point *E* (along the z-axis direction); " $\| \|_2$ " denotes the Euclidean norm of the vector; "×" represents the vector product; ***EC*** refers to the force arm vector of the moment at point *E* generated by $\boldsymbol{F_{CS}}$; and $\boldsymbol{n_{CS}}$ is the unit direction vector of $\boldsymbol{F_{CS}}$.

Subsequently, taking the mechanism *DNCS* as a unified system, the moment equilibrium equation at point *D* was established to solve the reaction force F_{NC} on the hydraulic cylinder:

$$F_{NC} = -\frac{\left\| \boldsymbol{F_{CS}} \times \boldsymbol{CD} \right\|_2}{\left\| \boldsymbol{ND} \times \boldsymbol{n}_{NC} \right\|_2} \tag{9}$$

where ***CD*** and ***ND*** are the direction vectors of the pendulum *CD* and the connecting rod *ND*, respectively; and $\boldsymbol{n_{NC}}$ represents the unit direction vector of the force on the connecting rod *NC*.

Finally, the output force F_{MN} of the hydraulic cylinder *MN* was obtained:

$$F_{MN} = F_{NC} \cos\delta \tag{10}$$

where δ refers to the rotation angle from the connecting rod *CN* to the hydraulic cylinder *MN*.

V. Integrated Leg Optimization Model

A. Design variables

By changing the configuration of the thigh linkage mechanism to reduce the peak force of the hydraulic cylinder *MN*. This involved altering the horizontal coordinate of joint point *N*, as well as the horizontal and vertical coordinates of joint points *C*, *D*, and *F*. They served as the design variables. In this case, the design variables could be expressed as:

$$\boldsymbol{x} = \{y_N, x_C, y_C, x_D, y_D, x_F, y_F\}^{\mathrm{T}} \tag{11}$$

B. Objective function

The objective function was defined as the peak force of the hydraulic cylinder *MN* in the working range.

$$f(x) = \max(F_{MN}) \tag{12}$$

C. Constraint conditions

1) Lower bound of rod length

The rod *NC* should be designed to incorporate a single-axis force sensor, ensuring that its length accommodated the necessary space for the sensor's installation.

$$L_{NC} \geq L_{\min} \tag{13}$$

where $L_{\min}$ represents the minimum length of the connecting rod *NC* determined by the size of the force sensor.

2) Monotonicity of mechanism motion

For precise control of the hydraulic cylinder with an increased swing angle *θ*, the movement of the hydraulic cylinder *MN* must be monotonic. This indicated that as the cylinder extended within its specified working range, the swing angle *θ* of the thigh should consistently increase.

$$\frac{\mathrm{d}\theta}{\mathrm{d}L_{MN}} > 0 \tag{14}$$

3) Anti-interference requirements

a) To prevent the movement of the connecting rod *NC* and the sliding sleeve of the hydraulic cylinder *MN* from interfering, the rotation angle δ of the connecting rod *NC* to the hydraulic cylinder *MN* should not exceed the maximum permissible value $\delta_{\max}$.

$$\delta \leq \delta_{\max} \tag{15}$$

b) A bearing should be installed at point *F*, and the included angle α between *ES* and *EI* should be maintained not less than the minimum permissible value $\alpha_{\min}$ to prevent interference with the installation space and the internal mechanism layout within the thigh.

$$\alpha \geq \alpha_{\min} \tag{16}$$

c) As the thigh *EFI* moved within the working range, the following requirement should be emphasized to prevent interference between the pendulum *CD* and the joint point *E*, and to maintain a safety distance *d*:

$$\frac{\left\| \boldsymbol{DE} \times \boldsymbol{DC} \right\|_2}{L_{CD}} \geq \frac{1}{2} w_{CD} + r_E + d \tag{17}$$

where ***DE*** denotes the position vector of *DE*, and ***DC*** represents the direction vector of pendulum *CD*. The left side of the inequality is the vertical distance between the joint point *E* and the pendulum *CD*. L_{CD} refers to the length of the pendulum *CD*; w_{CD} denotes the width of the pendulum *CD*; and r_E is the radius of the bearing at point *E*.

d) To avoid interference with the rest of the machine, the horizontal distance between points *M* and *E* should be controlled during installation and operation.

$$L_{ME} \leq L_{ME}^{\max} \tag{18}$$

e) Joint point *D* requires the installation of a joint bearing, and joint point *E* should be furnished with a dynamic sealing structure. Hence, it is essential to ensure that the distance between points *D* and *E* is greater than the sum of their respective radii to properly accommodate these components.

$$L_{ED}^{\min} \geq r_D + r_E \tag{19}$$

VI. Example Analysis

During the robot's walking motion, the swing angle *θ* of the thigh *EFI* and the drive moment M_E at joint point *E* were simulated and measured for each operating condition. $\theta \in [8^\circ, 55^\circ]$ for the robot walking on flat ground, while $\theta \in [55^\circ, 64^\circ]$ when climbing a 25° slope. The value of the driving moment was set according to the performance requirements of the robot, which varied with the swing angle *θ*. The final values of the drive moment at joint point *E* within the swing angle $\theta \in [0^\circ, 105^\circ]$ are shown in Fig. 5.

Grounded in the layout of the original thigh linkage mechanism, the force exerted by the hydraulic cylinder *MN* was calculated as the swing angle *θ* changed.

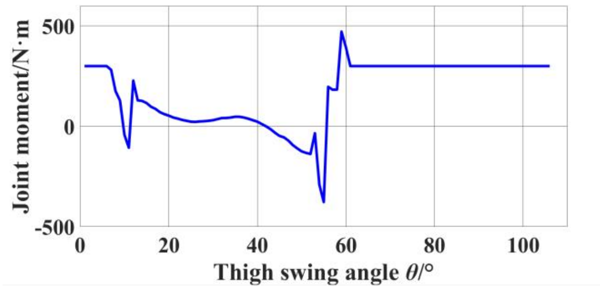

Fig. 5 Driving moment at joint point E

Fig. 6 presents the magnitude of the force of the hydraulic cylinder *MN*. At a swing angle θ of 58°, the hydraulic cylinder *MN*'s thrust force was at its peak, amounting to 8383.9 N. Conversely, at a swing angle θ of 54°, the cylinder's pull force was maximized, reaching 6592.9 N. At this time, the hydraulic cylinder *MN* failed to meet the performance requirements of the extreme working conditions.

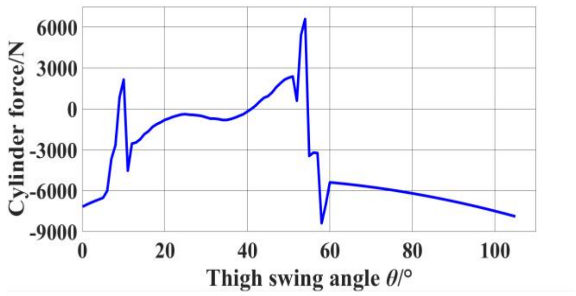

Fig. 6 Cylinder force before optimization

Considering both the working range requirements of the thigh mechanism and the spatial limitations of the entire machine's installation space, the constraints of the optimized design were established as:

$$\begin{cases} f(x) = \max(F_{MN}) \\ \textbf{s.t.} \\ \quad \delta \le 15^\circ \\ \quad \alpha \ge 7^\circ \\ \quad L_{NC} \ge 70 \\ \quad L_{ME} \le 450 \\ \quad L_{ED} \ge 33 \\ \quad \dfrac{\mathrm{d}\theta}{\mathrm{d}L_{MN}} > 0 \\ \quad \dfrac{\left\| \boldsymbol{DE} \times \boldsymbol{DC} \right\|_2}{L_{CD}} \ge 33 \end{cases} \tag{20}$$

where the rotation angle δ does not exceed 15°; the included angle α should be kept as least 7°; the length of the connecting rod *NC* should be no less than 70 mm; the distance of *ME* is no more than 450 mm; the distance of *ED* is no less than 33 mm; and the distance between the pendulum rod *CD* and the joint point *E* should be no less than 33 mm.

The coordinates of each point of the original and optimized mechanism are shown in Table I. Meanwhile, Fig. 7 compares the original mechanism configuration and the optimized mechanism configuration.

TABLE I
COORDINATES OF POINTS OF THE ORIGINAL AND OPTIMIZED THIGH LINKAGE MECHANISM

Joint points	Original/mm	Optimized/mm
M	(40, -442)	(40, -448)
N	(40, -149)	(40, -136)
C	(70, -32)	(66, -37)
D	(-10, -40)	(-23, -48)
E	(0, 0)	(0, 0)
F	(39, 31)	(58, 32)
I	(104, 386)	(104, 386)

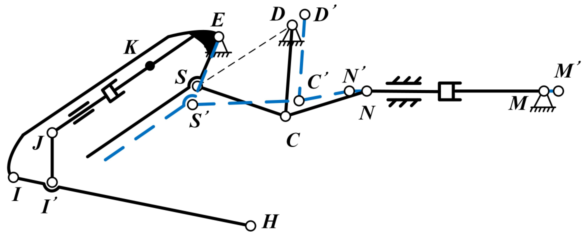

M, N, C, D, E, S, I - coordinates of joint points of the original mechanism configuration
M′, N′, C′, D′, E, S′, I′ - coordinates of joint points of the optimized mechanism configuration
Fig. 7 Original and optimized mechanism configuration

As depicted in Fig. 8, the comparison curves of hydraulic cylinder force between the original and optimized mechanisms presented a reduction in both the maximum thrust and pull forces exerted by the hydraulic cylinder. Upon optimization, the maximum hydraulic cylinder pulling force was 5542.3 N at $\theta = 54^\circ$, and the maximum hydraulic cylinder thrust force was 7061.2 N at $\theta = 58^\circ$. The comparison revealed that upon optimization, the hydraulic cylinder's thrust and pulling forces were reduced by 15.78% and 15.94%, respectively. The force of the hydraulic cylinder *MN* before and after optimization is illustrated in Table II.

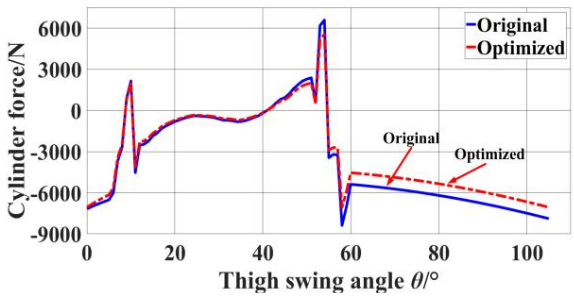

Fig. 8 Comparison of hydraulic cylinder forces of the original and optimized mechanism

TABLE II
PEAK OUTPUT FORCE OF THE HYDRAULIC CYLINDER MN OF THE ORIGINAL AND OPTIMIZED MECHANISM

	Original/N	Optimized/N	Reduced percentage
Maximum thrust force	8383.9	7061.2	15.78%
Maximum pulling force	6592.9	5542.3	15.94%

VII. VALIDATION OF OPTIMIZATION EFFECTS BASED ON EXPERIMENT

Herein, a suspended swing experiment on the integrated leg mechanism was conducted, and verified the effectiveness of the integrated leg kinematic model and the optimized model by comparing the measured hydraulic cylinder force with the calculated hydraulic cylinder force from the integrated leg kinematic model. The strain electrical measurement was conducted on key parts to obtain the actual stress distribution and verify whether the leg mechanism can meet the strength requirements.

A. Platform of the integrated leg mechanism

As shown in Fig. 9, the single leg experimental bench consisted of three parts, including a sliding support, a vertical slide rail, and the integrated leg mechanism. The single leg experimental bench retained the pitch degrees of freedom of the thigh and shank, enabling the longitudinal swing of the leg mechanism. The leg mechanism frame was fixed on a sliding support, ensuring the height variation of the leg mechanism.

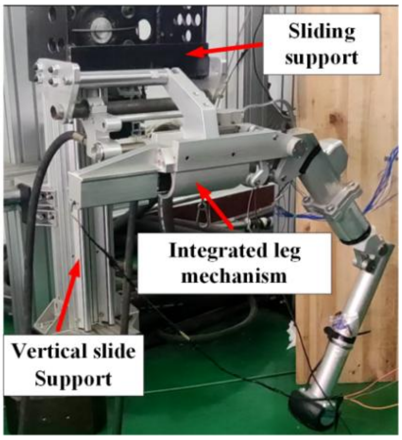

Fig. 9 Single leg experimental platform

The power mechanism of the single leg experimental platform was the ground hydraulic station, which provided a maximum hydraulic cylinder force of 18 MPa and a maximum stroke of 72 mm.

In the integrated leg mechanism, the thigh hydraulic cylinder was integrated using a displacement sensor, and a force sensor was installed at the connecting rod *CS*. In this case, the operating parameters of the thigh cylinder could be better measured. A single-axis force sensor model M3624A was used on the connecting rod *CS.*

B. The suspened swing experiment

The motion conditions of thigh suspended swing were set up, encompassing parameters like running velocity, the lengths of the thigh and calf cylinders, and the dwell time. As shown in Fig. 10, the thigh swing condition facilitated to maintain the shank joint angle at 54.6°, and to ensure the endurance of 2 seconds when the thigh joint angle shifted to 15°, 35°, 55°, 75°, 85°, and 90°, respectively. Subsequently, the thigh joint angle was adjusted to 15° again to initiate the next cycle of motion, and a total of 3 cycles of motion were performed.

Fig. 11 shows the parameter changes of the force sensor within 1 cycle. Then, the corresponding parameters were substituted into the kinematic model, and the force on the connecting rod *CS* was calculated. Following that, the output value of the kinematic model was compared with the experimental data to verify the effectiveness of the kinematic analysis. The comparison of the two data is shown in Table III.

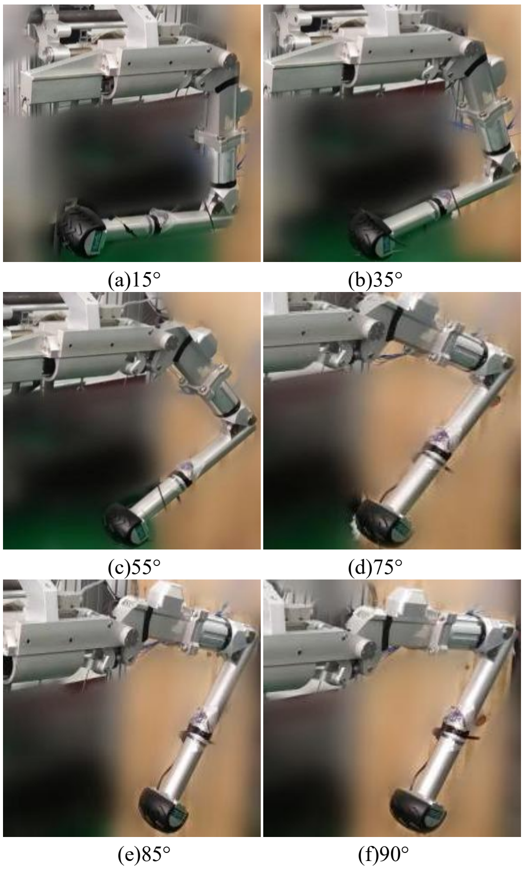

Fig. 10 The motion conditions of thigh suspened swing

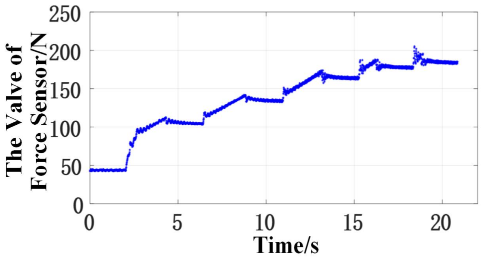

Fig. 11 Experimental data of thigh swing of physical prototyper

TABLE III
FORCE COMPARISON OF THE CONNECTING ROD CS

Thigh joint angle/°	Measured force/N	Model calculation force /N
15.0°	43.7	37.9
35.0°	105.5	92.3
45.0°	141.2	139.1
75.0°	170.7	180.3
85.0°	184.5	198.1
90.0°	191.1	205.8

In the kinematic analysis of the integrated leg mechanism, the gravitational effects of components like servo valves and hydraulic lines were overlooked. This oversight led to the unstable force readings. These vibrations contributed to discrepancies between the force values predicted by the kinematic model and those measured experimentally. However, the maximum error was found to be 13.3%, confirming the efficacy of the integrated leg mechanism kinematic model within an acceptable range.

Upon the completion of the thigh swing condition, the tester readjusted the motion condition of the leg mechanism, as shown in Fig. 12. The thigh joint angle was kept at 75°, and the shank joint angle was stabilized at 41.4°, 66.3°, 91.1°, and 105° for 2 seconds, respectively. Then, the shank joint angle was adjusted back to its initial value, and the next cycle of motion began. Three cycles of motion were conducted, and the displacement sensor and force sensor values were collected.

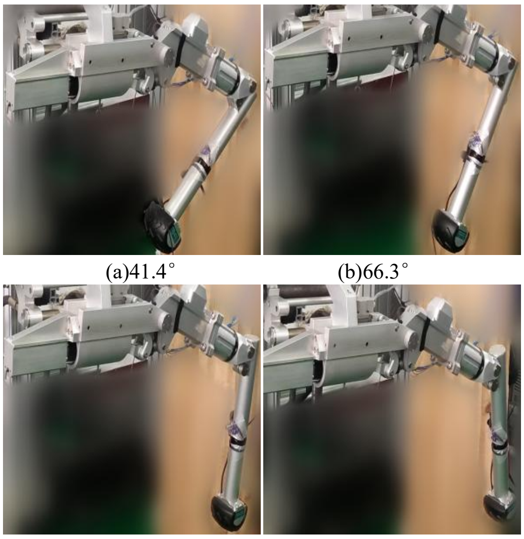

(a)41.4° (b)66.3° (c)91.1° (d)105°

Fig. 12 The motion conditions of shank suspened swing

Fig. 13 shows the data on the force sensor of the shank cylinder within one cycle. Similarly, the average force of the shank cylinder was calculated over three cycles, resulting in data for four distinct postures during the suspension swing. The cylinder lengths for these postures were then input into the dynamic model, which then provided the corresponding forces exerted by the shank cylinder. The final comparison between the dynamic model and actual measured data during leg suspension swing is shown in Table IV.

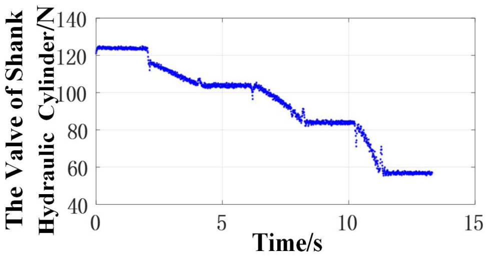

Fig. 13 Experimental data of shank swing of physical prototype

TABLE IV
COMPARISON OF SHANK CYLINDER FORCE VALUES

Shank joint angle/°	Measured force/N	Model calculation force /N
41.4°	123.8	116.6
66.3°	103.9	95.7
91.1°	84.1	76.1
105.0°	57.0	50.3

By comparing forceand considering the differences between the actual physical prototype and the dynamic model modeling, the maximum relative error was found to be 11.8% at a shank joint angle of 105°, while the absolute error was only 6.7 N. Within an acceptable range, it was verified that the dynamic model could effectively solve the shank cylinder force.

C. *Strain electrical measurement experiment*

Due to the complex force distribution during the operation of the integrated leg mechanism, uniaxial strain gauges and three-axis 45° strain gauges were employed to ensure measurement accuracy. For each uniaxial strain gauge measuring point, the direction of the principal stress σ was known, and the measured strain was the principal strain of the measuring point. When the principal strain ε was measured, Hooke's law could be directly used to calculate the stress value at the measurement point position [18]-[20].

TABLE V
PARAMETERS OF STRAIN GAUGE AND STRAIN ROSETTE

	Resistance/Ω	Sensitivity coefficient
BE-120-3AA-P150 Strain gauge	120.0±0.1	2.17±1%
BE-350-3CA-P100 Strain rosette	350.5±0.3	2.17±1%

The hinge points of the integrated leg mechanism were relatively fragile compared to other parts, presenting high stress. More critically, it was also an important part for transmitting force. Consequently, the measurement points were mainly arranged near the hinge points. As shown in Fig. 14, the numerical numbers (1-4) indicate the location of the strain gauges to be pasted, necessitating a total of four strain gauges. Meanwhile, the letter number (a-g) represents the position of the strain rosettes pasting, requiring a total of 7 strain rosettes.

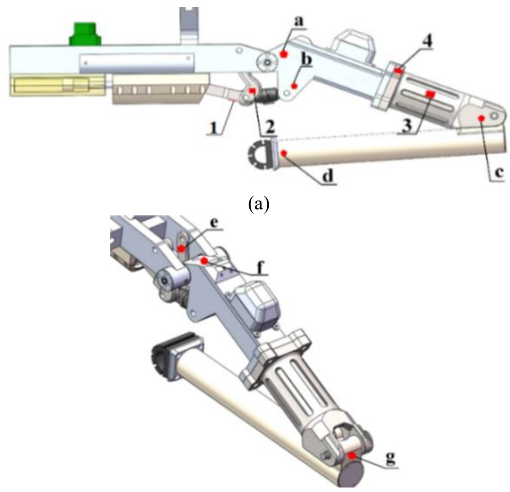

(a)

(b)

Fig. 14 Position of test points

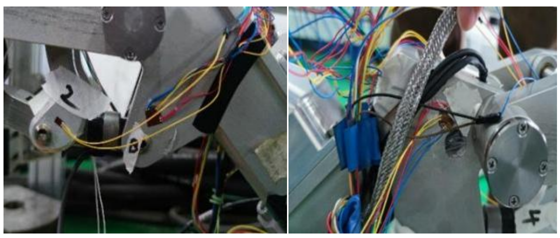

Fig. 15 Paste diagram of strain gauges and strain rosettes

Once it was confirmed that the strain gauges (strain rosettes) at each measuring point met the experimental requirements, the testing system was preheated and cleared to zero in preparation for data collection, while the leg mechanism was suspended. As shown in Fig. 16 (a), a weight of 9.16 kg was placed on the sliding support. In the initial state, the length of the thigh hydraulic cylinder was 269.8 mm, while that of the shank hydraulic cylinder was 215 mm. The length of the thigh hydraulic cylinder was adjusted to 266.9 mm, while that of the shank hydraulic cylinder was changed to 232 mm, kept for 10 seconds. Then, the length of the thigh hydraulic cylinder was adjusted again to 264 mm, and that of the shank hydraulic cylinder to 255 mm. After a 10-second hold, the system was adjusted back to its initial state, and the entire procedure was repeated. Data from the entire process were collected.

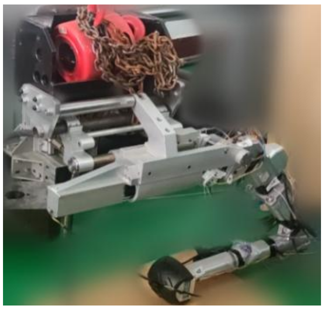

(a)Posture 1

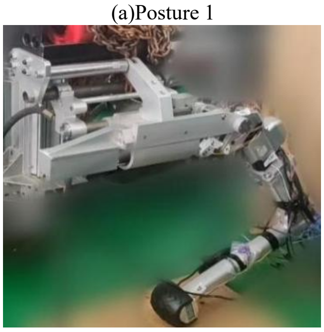

(b)Posture 2

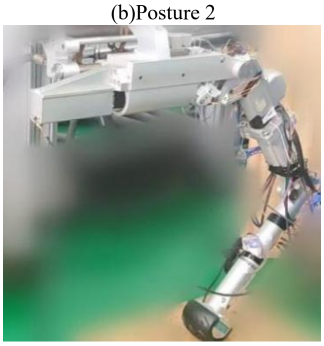

(c)Posture 3

Fig. 16 Working condition of squatting with load

A total of 3 cycles of motion were conducted, with 11 measurement points collected from each group. Once the data for each operating condition had stabilized, strain values at the measurement points were recorded, and the average strain values across different postures within three cycles were determined. The tested component was 7075 aluminum alloy, with an elastic modulus of 71.7 GPa, Poisson's ratio v = 0.33, and a yield strength of 455 MPa. The Mises stress value at the measurement point position was calculated according to Hooke's law. The experimental data of the measurement points are presented in Fig. 17 and Table VI.

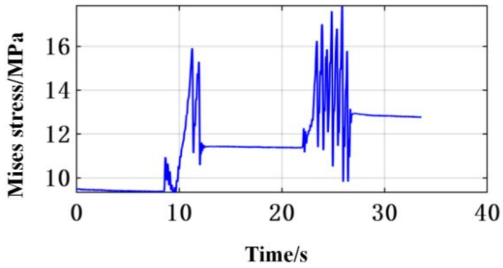

(a)Test point 3

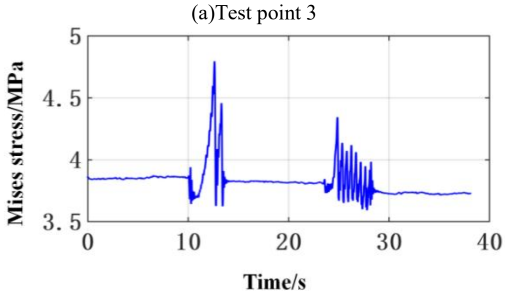

(b)Test point a

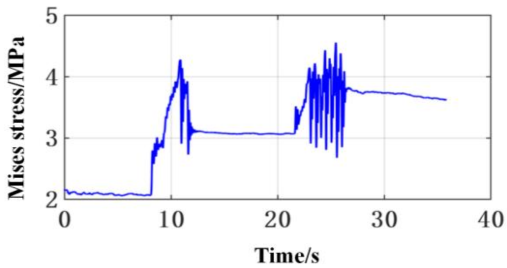

(c)Test point c

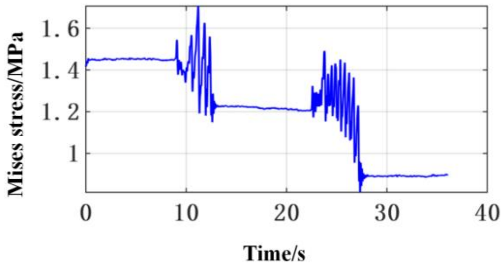

(d)Test point d

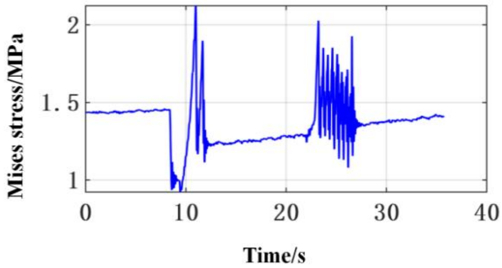

(e)Test point f

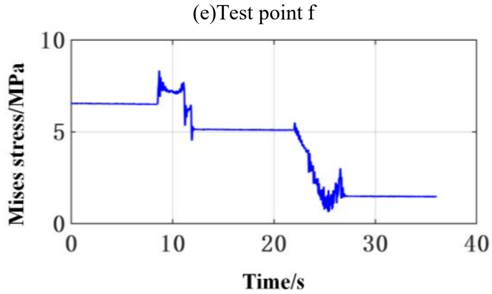

(f)Test point g

Fig. 17 The Mises stress at the test point

TABLE VI
STRESS OF EACH MEASURING POINT OF LEG MECHANISM

Point	posture 1/MPa	posture 2/MPa	posture 3/MPa
3	9.45	11.41	12.84
a	2.08	3.07	3.74
c	1.45	1.22	0.89
d	3.86	3.82	3.72
f	7.22	5.03	2.38
g	1.46	1.33	1.40

According to Fig. 17, neglecting the small stress at points 1, 2, 4, b, and e, point 3 had the maximum stress when the three postures were stable. The stress fluctuated due to the sliding of the foot against the ground during the squatting motion of the leg mechanism, peaking at approximately 18 MPa.

Following the weighing process, the total weight of the single leg platform was approximately 36 kg. When installed on the entire machine, the curb weight was 180 kg, and the design maximum load was roughly 70 kg. During the motion process, the gait characteristics and impact load of the robot were considered, and the maximum load on a single leg was about the full load mass of the entire machine. By comparing the numerical relationship between the load on a single leg platform and the load on a single leg of the complete machine, it was estimated that the maximum stress on the connecting rod of the integrated leg mechanism was approximately 125 MPa. The yield strength of the material was compared, further confirming that the integrated leg mechanism satisfied the strength requirements and left a certain safety margin.

VIII. CONCLUSION

Herein, the configuration of a innovative integrated leg for legged robots was investigated and optimized. Initially, an explicit parameter equation regarding the dynamic coordinates of the hinge joints was established using vector algebra and linear transformation methods, and the force of the hydraulic cylinder was accurately calculated. Subsequently, in order to minimize the force of hydraulic cylinder, the optimization model of the integrated leg mechanism was established. Ultimately, the effectiveness of the mechanism optimization was verified through experiments. The research conclusion could be listed as follows:

1) Utilizing the vector algebra and linear transformation methods, the hydraulic cylinder force of the leg mechanism could be derived by the plantar force. The original leg mechanism exhibited excessive hydraulic cylinder forces, resulting in inadequate performance during extreme tasks like rising from a reclined position and traversing steep slopes while the entire machine was down.

2) In determining the plantar force, the hydraulic cylinder force of the leg mechanism was related to the positions of the hinge points. By changing the position of the hinge points, the peak force of the hydraulic cylinder could be reduced, and the working performance of the leg mechanism could be improved.

3) The effectiveness of the dynamic model and the effect of the optimization were both confirmed through suspension experiments. The error of the dynamic model fell within a reasonable range, and the optimized hydraulic cylinder force was reduced by 15%.

4) The actual stress distribution of the leg mechanism was obtained through strain electrical testing experiments, and it was found that the leg mechanism can meet the strength requirements.

REFERENCES

[1] Picardi G, Chellapurath M, Iacoponi S, et al. "Bioinspired underwater legged robot for seabed exploration with low environmental disturbance," *Science Robotics*, vol. 5, pp. 1012-1026, 2020.

[2] Kim T J, Won D H, Kwon O, et al. "Design and Control of a Hydraulic Driven Quadruped Walking Robot," *Journal of Korea Robotics Society*, vol. 2, no. 4, pp. 353-360, 2007.

[3] Mosher R S. "Test and evaluation of a versatile walking truck," *Proceedings of Off-Road Mobility Research Symposium*, pp. 359-379, 1968.

[4] Raibert M, Blankespoor K, Nelson G, et al. "BigDog, the rough-terrain quadruped robot," *Proceedings of the 17th IFAC World Congress. Oxford, UK: IFAC*, pp. 10822-10825, 2008.

[5] Sasmeeta T ,Sanjeev G. "Rough terrain quadruped robot- BigDog," *Materials Today: Proceedings*, vol. 81, pp. 481-485, 2023.

[6] Semini C, Tsagarakis N G, Guglielmino E, et al. "Design of HyQ - A hydraulically and electrically actuated quadruped robot," *Proceedings of the Institution of Mechanical Engineers, Part I: Journal of Systems and Control Engineering*, vol. 225, no. 6, pp. 831-849, 2011.

[7] Semini C. "HyQ-Design and development of a hydraulically actuated quadruped robot," *Genoa: University of Genoa*, 2010.

[8] Li M, Guo Y, Jiang Z, et al. "A simplified model control method for the Trot gait of a quadruped robot," *Mechanics and Electronics*, vol. 10, pp. 3-7, 2012.

[9] Jiang Z, Li M, Guo W. "Running control of a quadruped robot in trotting gait," *IEEE Conference on Robotics, Automation and Mechatronics. Piscataway, USA: IEEE*, pp. 172-177, 2011.

[10] Zhang T, An H, Ma H. "Joint torque and velocity optimization for a redundant leg of quadruped robot," *International Journal of Advanced Robotic Systems*, vol. 14, no. 5, pp. 1-12, 2017.

[11] Wang L, Meng F, Kang R, et al. "Design and Implementation of Symmetric Legged Robot for Highly Dynamic Jumping and Impact Mitigation," *Sensors*, vol. 21, no. 20, pp. 6885, 2021.

[12] Chai H, Meng J, Rong X, et al. "Design and implementation of a high-performance hydraulically driven quadruped robot SCalf," *Robotics*, vol. 36, no. 4, pp. 385-391, 2014.

[13] Jaemin L, Junhyeok A, Donghyun K, et al. "Online Gain Adaptation of Whole-Body Control for Legged Robots with Unknown Disturbances," *Frontiers in Robotics and AI*, vol. 8, pp. 788902, 2022.

[14] Immanuel P, Jeanette P, Charles A B, et al. "Development of a Segmented Body Serpent Robot with Active Head Floating Control," *Engineering Letters*, vol. 31, no. 4, pp. 1928-1943, 2023.

[15] Zong H, Zhang J, Zhang K, et al. "Research status and development trend of hydraulic quadruped robot components and hydraulic systems," *Hydraulics and Pneumatics*, vol. 45, no. 8, pp. 1-16, 2021.

[16] Suphanut K, Hiroshi H. "Optimization on mechanical structure for material nonlinearity based on proportional topology method," *Journal of Advanced Simulation in Science and Engineering*, vol. 6, no. 2, pp. 354-366, 2019.

[17] Poningsih, Poltak S, Muhammad Z, and et al. "Optimization Model for Outpatient Services Capacity Management in Different Patient Conditions and Diseases," *IAENG International Journal of Computer Science*, vol. 51, no. 3, pp. 260-266, 2024.

[18] Cai Y W, Li S C, Wu M M. "Research on the Electrical Measurement Method for Extreme Stress of Eccentric Pull Rod," *Journal of Jiangsu Normal University (Natural Science Edition)*, vol. 32, no. 3, pp. 50-53, 2014.

[19] Brasier R. I., Dove R. C. "Use of electrical-resistance strain elements in three-dimensional stress analysis," *Experimental Mechanics*, vol. 1, no. 6, pp. 186-191, 1961.

[20] Tang S L. "The application and main error analysis and correction of resistance stress testing technology," *Modern Manufacturing Technology and Equipment*, vol. 5, pp. 152-153, 2018.